

MDPI

Article

# Hysteresis in Organic Electrochemical Transistors: Relation to the Electrochemical Properties of the Semiconductor

Raufar Shameem †,‡, Lukas M. Bongartz, Anton Weissbach , Hans Kleemann and Karl Leo \*

Dresden Integrated Center for Applied Physics and Photonic Materials (IAPP), Technische Universität Dresden, Nöthnitzer Str. 61, 01187 Dresden, Germany

- \* Correspondence: karl.leo@tu-dresden.de
- † Current address: Laboratory of Organic Electronics, Department of Science and Technology, Linköping University, 602 21 Norrköping, Sweden.
- ‡ Current address: Bio- and Organic Electronics, RISE Research Institutes of Sweden, 602 33 Norrköping, Sweden.

Abstract: The ability to bridge ionic and electronic transport coupled with large volumetric capacitance renders organic electrochemical transistors (OECTs) ideal candidates for bioelectronic applications. Adopting ionic-liquid-based solid electrolytes extends their applicability and facilitates large-area printable productions. However, OETCs employing solid electrolytes tend to show a pronounced hysteresis in the transfer curve. A detailed understanding of the hysteresis is crucial for their accurate characterizations and reliable applications. Here, we demonstrated fully photopatternable poly(3,4-ethylenedioxythiophene):tosylate (PEDOT:Tos)- based OECTs incorporating the ionic liquid [EMIM][EtSO<sub>4</sub>] in a solid electrolyte (SE). The PEDOT:Tos films deposited through vapor phase polymerization (VPP) were annealed for different durations after the polymerization step. Upon rinsing with ethanol and the deposition of the SE, the OECTs made of these films showed impressive bias stress stability under prolonged operation cycles, a high switching ratio, a low threshold voltage, and a high transconductance. Furthermore, by taking transfer measurements with different sweep rates, we revealed two distinct regimes of hysteresis: kinetic hysteresis and non-kinetic hysteresis. We observed pronounced changes in these regimes after annealing. Finally, impedance spectroscopy exhibited that the PEDOT:Tos turned from a Faradaic to a non-Faradaic response through annealing, explaining the observed hysteresis changes in both regimes.

**Keywords:** organic electrochemical transistors; organic mixed ionic–electronic conductors; hysteresis; vapor phase polymerization; bias stress

# check for updates

Citation: Shameem, R.; Bongartz, L.M.; Weissbach, A.; Kleemann, H.; Leo, K. Hysteresis in Organic Electrochemical Transistors: Relation to the Electrochemical Properties of the Semiconductor. *Appl. Sci.* **2023**, 13, 5754. https://doi.org/10.3390/ app13095754

Academic Editor: Carolina Belver

Received: 4 April 2023 Revised: 27 April 2023 Accepted: 28 April 2023 Published: 7 May 2023



Copyright: © 2023 by the authors. Licensee MDPI, Basel, Switzerland. This article is an open access article distributed under the terms and conditions of the Creative Commons Attribution (CC BY) license (https://creativecommons.org/licenses/by/4.0/).

## 1. Introduction

Owing to their ability to transduce both electronic and ionic signals, organic electrochemical transistors (OECTs) are ideal candidates for bioelectronics [1,2], sensors [3,4], and neuromorphic applications [5–8]. OECTs are three-terminal devices comprising an organic mixed ionic electronic conductor (OMIEC) [9] as the channel between the source and drain electrode. An electrolyte acts as the ion reservoir between the channel and gate electrode. When the drain–source bias ( $V_{DS}$ ) is fixed, a changing gate–source voltage ( $V_{CS}$ ) dictates the flow of the mobile ions between the OMIEC channel and the electrolyte. These ions, in turn, change the doping states and the conductivity ( $I_D$ ) of the OMIEC channel [10]. As a result, OECTs are volumetric devices, which grants them a high transconductance (high amplification), allowing them to operate at relatively low voltages [11].

Various conjugated polymers are suitable as the channel materials of OECTs [12]. One polymer of particular interest that allows precision control over device properties is poly(3,4-ethylenedioxythiophene):tosylate (PEDOT:Tos) [13,14]. A popular method to deposit PEDOT:Tos is vapor phase polymerization (VPP). Although various variations are possible [15], VPP typically follows the routine of surface preparation by an oxidant, polymerization in

Appl. Sci. **2023**, 13, 5754

vacuum, post-polymerization annealing, and the removal of residuals. Traditionally, the electrolyte used for gating incorporates water with salts (i.e., liquid electrolyte), which can evaporate and contaminate easily and is inconvenient for all-printed applications. Ion gels, a composite material comprising an ionic liquid in a complex polymer matrix [16] (also referred to as solid electrolyte or SE), are printable [17], scalable [18], and photopatternable [19].

The typical figures of merit of OECTs, such as the transconductance, switching ratio, and threshold voltage, are extracted from the transfer curve measurements. It has been shown that OECTs employing an SE have a pronounced hysteresis in the transfer curves [19]. In other words, the device gives two sets of data depending on whether the transfer curve measurement is taken from the ON to the OFF state and vice versa. Previous work has tried to explore the origin of hysteresis from different perspectives where the explanations differ significantly. Kaphle et al. attributed hysteresis to an incomplete movement of ions [20], which explains the change in hysteresis with changing gate–source voltage scan rates. However, an ionic-movement-based explanation fails to explain a saturating hysteresis (i.e., a hysteresis that sustains even for a sufficiently slow scan rate). Winther-Jensen et al. argued that hysteresis could be adjusted by controlling the degree of polymer collapse by modifying the concentration of polytetrahydrofuran (PTHF) in the PEDOT:Tos blend [13]. Ji et al. later showed that such a change is instead connected to the trapping of cations by PTHF [14]. However, none of these theories explain the presence of hysteresis in PEDOT:Tos-based OECTs without any PTHF additive. Regardless of the explanations, it is safe to assume that multiple factors might contribute to hysteresis in OECTs. In particular, the influence of defect states on hysteresis remains elusive.

Here, we introduce a fully photopatternable PEDOT: Tos OECT employing a solid electrolyte with [EMIM][EtSO<sub>4</sub>] as the ionic liquid. Contrary to conventional patterning via parylene peel-off, photolithography coupled with dry etching is cleaner and less complex [21]. We annealed the deposited PEDOT: Tos film for different durations before washing it with ethanol. Upon residual removal from the deposited films and SE deposition, the resulting OECTs showed impressive bias stress stability under prolonged operation. By varying the gate–source voltage ( $V_{\rm GS}$ ) scan rate, we revealed two distinct regimes of hysteresis distinguishable by their kinetics. We named them kinetic and non-kinetic hysteresis depending on whether they change by change in the  $V_{\rm GS}$  scan rate. We observed an increasing kinetic hysteresis in the devices with increased thermal annealing. However, the strength of the non-kinetic hysteresis and its onsets remain curious. From the impedance measurements, we observed that PEDOT: Tos switched from a non-polarizable (Faradaic) to a polarizable (non-Faradaic) behavior upon thermal annealing, explaining the evolution of the hysteresis over different scan rates. We speculated that annealing caused a demixing in PEDOT: Tos, causing ion trapping in the different phases of the material.

#### 2. Materials and Methods

The sample fabrication and characterization were carried out in a cleanroom environment. The OETCs involved in this work were a side-gated planar electrode configuration utilizing a three-stage photolithography patterning process (see Figure 1a). A glass substrate (1"  $\times$  1", 3 nm Cr and 50 nm Au) was spin-coated (60 s, 3000 rpm; Sawatec SM-180-BT, Sax, Switzerland ) with the photoresist AZ 1518 (MicroChemicals GmbH, Ulm, Germany) followed by baking on a hotplate (60 s, 110 °C; Sawatec HP-150, Sax, Switzerland). The illumination of the electrode pattern ensued in a mask aligner (10 s, I-line 365 nm, 167 W; SÜSS Microtec AG, Garching, Germany). The development of AZ 1518 (60 s, AZ 726 MIF; MicroChemicals GmbH, Ulm, Germany) and etching of Au (60 s; 10% diluted aqueous; Merck KGaA, Darmstadt, Germany), respectively, produced the desired electrode pattern on the glass substrate.

The second stage of photolithography started with the deposition of PEDOT:Tos. We followed a five-step base-inhibited VPP process [22] with some modifications. First, the substrate was spin-coated (15 s, 1500 rpm) with the reactants Fe(III):Tos (324 mg; Sigma Aldrich, Taufkirchen Germany), pyridine (32  $\mu$ L; Alfa Aesar, Karlsruhe, Germany), and butanol (1.6 mL;

Appl. Sci. **2023**, 13, 5754 3 of 11

Acros Organics, Karlsruhe, Germany), followed by air drying for 30 min. The polymerization was carried out in a desiccation chamber (Gebr. Rettberg GmbH, Göttingen, Germany). A Petri dish containing EDOT (Sigma Aldrich, Taufkirchen Germany) was kept at the bottom of the desiccation chamber, while the substrate containing the reactants was set on a stage. The desiccation chamber was kept on a hotplate at 70 °C, which maintained the substrate temperature at around 50 °C (VOLTCRAFT IR 500-12S, Hirschau, Germany). The desiccation chamber was connected to a vacuum pump rated at 780 Pa. The equilibration time was 10 min, and the polymerization time was 1 h. The post-polymerization thermal annealing was carried out for 0, 1, and 4 h on a hotplate at 70 °C. Finally, the deposited PEDOT:Tos was carefully dipped in ethanol to remove any residuals.

Next, the substrate with the electrode pattern and the deposited polymer was spin-coated with an SL1 sacrificial layer (60 s, 3000 rpm; post-baking at 100 °C for 60 s; Orthogonal Inc., Rochester, NY, USA) [21] and photoresist AZ nLOF 2020 (60 s, 3000 rpm; post-baking at 110 °C for 60 s; MicroChemicals GmbH, Ulm, Germany). The illumination in the mask aligner (14 s, I-line 365 nm, 167 W; SÜSS Microtec AG, Garching, Germany) and post-baking followed (60 s, 110 °C). The resist was developed by AZ 726 MIF (60 s; MicroChemicals GmbH, Ulm, Germany), and the unprotected sacrificial layer was removed by spin coating (3000 rpm, increments of 15 s until undercut appeared) with HFE (3M Performance Chemicals, Nordrhein-Westfalen Germany). The final PEDOT:Tos pattern on the gate and channel was obtained by dry etching with oxygen plasma (300 s, 100 V bias, 50 W RF power, 30 Pa; Aurion VPA-14-01, Seligenstadt, Germany). The crosslinked resist and underlying SL1 were removed by keeping the substrate in the OSCoR Developer 103a (Orthogonal Inc.) overnight. The SE pattern was achieved by the same method reported earlier [19].

The thickness measurements were taken using a profilometer (Veeco Dektak 150, Aschheim, Germany). All electrical and impedance measurements were carried in a  $N_2$  glovebox (MBraun, Garching Germany). The electrical measurements were taken with two Keithley 236 SMUs (Oregon, United States) coupled with the software SweepMe! (Dresden, Germany). The impedance measurements were taken with Metrohm Autolab PGSTAT302N (Filderstadt, Germany) in the potentiostatic mode with an RMS amplitude of  $10\,\mathrm{mV}$  and without any DC offset. The scan range was from  $10^5$  to  $10^{-1}$  Hz, and the fitting was performed from  $10^4$  Hz (excluding the outliers at higher frequencies).

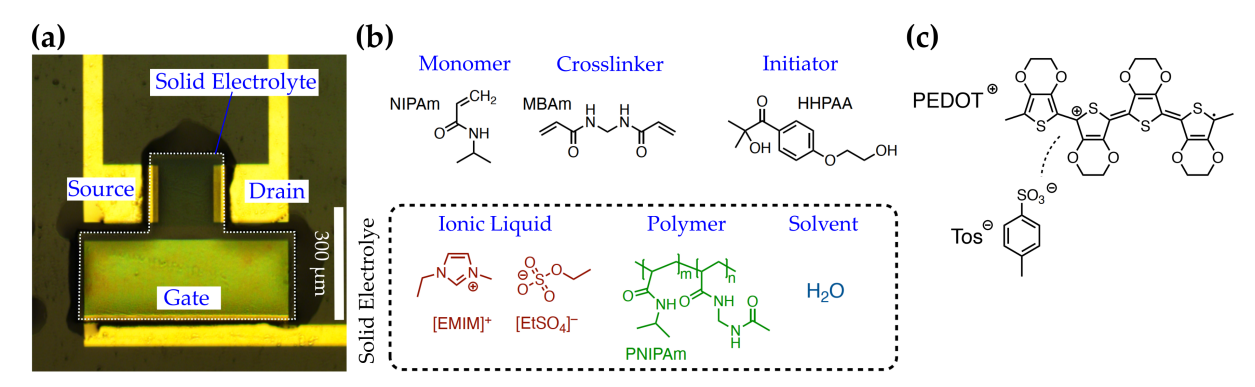


**Figure 1.** (a) Micrograph of a fabricated OECT; (b) the chemicals used as the solid electrolyte; (c) schematic of the OMIEC polymer PEDOT:Tos.

### 3. Results and Discussion

After polymerization in vacuum and before ethanol washing, the deposited PE-DOT:Tos films were annealed for 0, 1, and 4 h at 70 °C. Here, we report the preliminary comparisons of our fabricated PEDOT:Tos films and devices. Figure 1a shows a fabricated device, and Figure 1b,c depict the corresponding chemical composition of the SE and channel material, respectively. We observed an increasing film thickness and decreasing film conductivity (see Appendix A.1 Figure A1) with increasing annealing time, in line with the results of Zuber et al. [23]. According to this report, the film thickness increased due to further polymerization from the residuals, while the decreased conductivity (even with an

Appl. Sci. 2023, 13, 5754 4 of 11

increased doping level) was explained by the branching out of polymers. A pronounced hysteresis was noticeable in the transfer curves of the annealed devices. At a  $V_{GS}$  scan rate of  $175\, mV\, s^{-1}$ , the 0, 1, and 4 h-annealed devices showed ON–OFF  $(I_{ON,\,-1\,V}/I_{OFF,1.25\,V})$  ratios of  $2.50\times 10^4$ ,  $4.29\times 10^4$ , and  $2.06\times 10^4$ ; peak transconductances of 0.76, 0.66, and 0.26 mS; and threshold voltages of 0.31, 0.47, and 0.89 V, respectively (see Appendix A.2 Figure A2). The following section discusses the bias stress and ways to mitigate it. After that, we depict the two regimes of hysteresis over the  $V_{GS}$  scan rate in the 1 h-annealed device as a demonstration. In the final section, we evaluate the effect of post-polymerization thermal annealing in PEDOT:Tos.

## 3.1. Bias Stress and Recovery

The conductivities of the polymers decreased slightly after depositing the SE, which was indicative of partial polymer dedoping [24]. Therefore, we included a negative  $V_{\rm GS}$  voltage during the transfer curve measurements. The transfer curve sweeping was typically carried out from  $-1.0\,\rm V$  to  $1.25\,\rm V$ , then back to  $-1.0\,\rm V$  to scan the full switching potential of the device (i.e., including complete dedoping and redoping of the polymer; see Appendix A.3 Figure A3). A previous study showed that bias stress arose from the incomplete movement of ions between the SE and polymer [20]. Therefore, if the  $V_{\rm GS}$  scan rate (sweeping speed) is too slow or the  $V_{\rm GS}$  scan window is too large, then the bias stress will not be visible. Moreover, the drain–source voltage ( $V_{\rm DS}$ ) should also be small enough to avoid current stress (see Appendix A.4 Figure A4). We performed five-hundred successive transfer curve measurements (from purple to red gradient in Figure 2a). This measurement, lasting for about 6 h, showed some bias stress effect in our device (i.e., the shift of the transfer curves). Nevertheless, a recovery measurement after the bias stressing indicated that the device completely recovered even after prolonged operation. The latter reported measurements were taken after giving sufficient pauses to avoid bias stress.

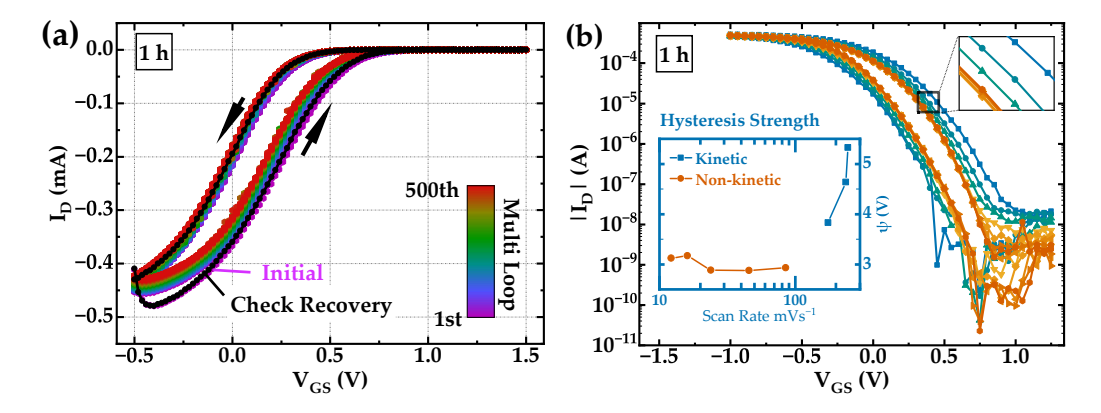


Figure 2. (a) Bias stress stability measurement in an OECT where the PEDOT:Tos film is annealed for 1 h at 70 °C. The measurement spans approximately six hours, with a recovery measurement showing no evidence of device degradation. (b) Demonstration of a scan-rate-dependent transfer curve measurement where the inlet shows the hysteresis strength  $\psi$  [19,25]. Such a measurement reveals two distinct regimes of hysteresis, which we name kinetic hysteresis (blue gradients) or non-kinetic hysteresis (orange gradients), depending on whether they change for a further reduction of the scan rates. Kinetic hysteresis at higher scan rates is related to the incomplete movement of ions, whereas non-kinetic hysteresis observed at lower scan rates results presumably from a combination of multiple factors. The channel width W, length L, and gate distance g are 150 µm, 150 µm, and 50 µm, respectively. The film thickness d for the bias stress measurement is 80 nm and for the scan-rate-dependent measurement is 119 nm. The drain–source voltage ( $V_{DS}$ ) is kept constant at  $-0.2 \, V$ . The scan speed for bias stress measurement is  $\approx 180 \, \text{mV s}^{-1}$ .

Appl. Sci. 2023, 13, 5754 5 of 11

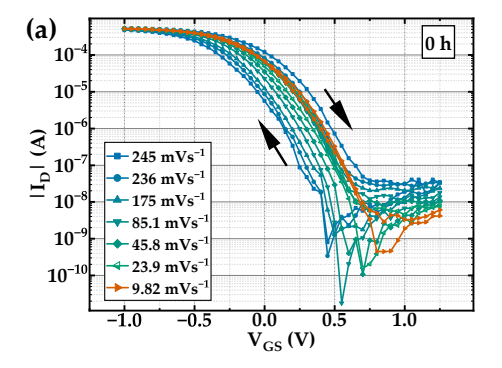
## 3.2. Regimes of Hysteresis

As the ions need to physically move to switch the device, the response time of the OECTs to a change of the input signal  $V_{\rm GS}$  is typically large. The response time also depends on parameters such as the ion mobility (conductivity of the electrolyte) or the distance between the channel and gate [1]. Therefore, the shape of the transfer curve (and the extracted parameters) depends closely on the  $V_{\rm GS}$  scan rate. We carried out a set of measurements with a fixed  $V_{\rm GS}$  step and different hold times to extract transfer curves with varying  $V_{\rm GS}$  scan rates (in units of mV s<sup>-1</sup>). The gate voltage was set at -1 V for 15–30 s before each transfer curve measurement to ensure that the polymer reached the maximum conducting state. Holding  $V_{\rm GS}$  at the beginning of each measurement also acted as a pause, allowing the cations to move completely out of the polymer to mitigate any bias stress effect. Nevertheless, the duration of these measurements with different scan rates was around 20 min, which is much shorter than the time scale on which we observed the bias stress instability (see Appendix A.5 Figure A5).

Figure 2b depicts the scan-rate-dependent transfer curve measurements for the OECT made from the 1 h-annealed PEDOT:Tos film. We utilized the  $\psi$  parameter to represent the hysteresis strength, which is the ratio of a pair of outputs  $I_D$  to the same input  $V_{GS}$ , integrated over the hysteresis window [19] (see Figure 2b inlet). The  $\psi$  parameter indicated that the hysteresis saturated at a scan rate of  $\approx\!85\,\text{mV}\,\text{s}^{-1}$  for the 1 h-annealed devices. We assumed that the kinetic hysteresis observable under a faster scan rate was indeed due to the incomplete movement of the ions, as shown earlier [20]. However, the nature of the inner non-kinetic hysteresis at lower scan rates was not trivial.

### 3.3. Effect of Thermal Annealing on Hysteresis

We report the scan-rate-dependent measurements for OECTs where the PEDOT:Tos was annealed for 0, 1, and 4 h. In Figure 3a-c, we show the transfer curves for different scan rates and annealing durations. Figure 3d shows the hysteresis strength  $\psi$  for these devices as a function of the scan rate. We observed a direct correlation between hysteresis strength and annealing time for a fixed V<sub>GS</sub> scan rate in the kinetic hysteresis regime. For example, at a scan rate of 175 mV s<sup>-1</sup>, the 0, 1, and 4 h-annealed devices showed a  $\psi$  value of 2.17, 2.93, and 7.42 V, respectively. However, the devices behaved curiously in the non-kinetic hysteresis regime. Firstly, the non-kinetic hysteresis for the non-annealed device (0 h) was significantly lower ( $\psi = 0.51 \text{ V}$ ) than for the annealed devices, where  $\psi$  reached a value of approximately 3 V (note that  $\psi$  is a logarithmic quantity and, hence, the difference between the annealed and non-annealed devices was very large). Secondly, the non-kinetic hysteresis for the 1 and 4 h-annealed devices were almost similar at around  $\psi = 3 \text{ V}$ , indicating that the effect of annealing was almost complete after 1 h. Finally, the onset of the non-kinetic hysteresis did not show any specific dependence on the scan rate (e.g., the onset of non-kinetic hysteresis for the 0, 1, and 4 h-annealed devices were at 9.82, 85.1, and 7.05 mV s<sup>-1</sup>, respectively). This aspect reflected the situation that the transition from the non-kinetic to the kinetic hysteresis was governed by the time constant of ion movement, which may depend significantly on the thickness and conductivity of the solid electrolyte.



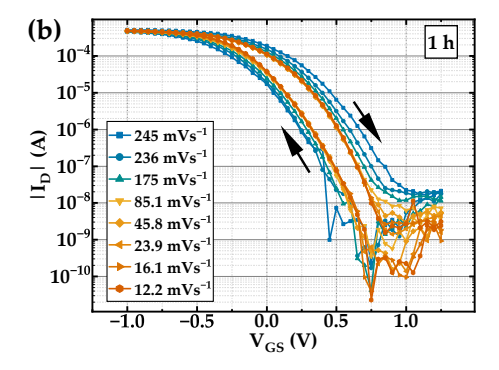


Figure 3. Cont.

Appl. Sci. 2023, 13, 5754 6 of 11

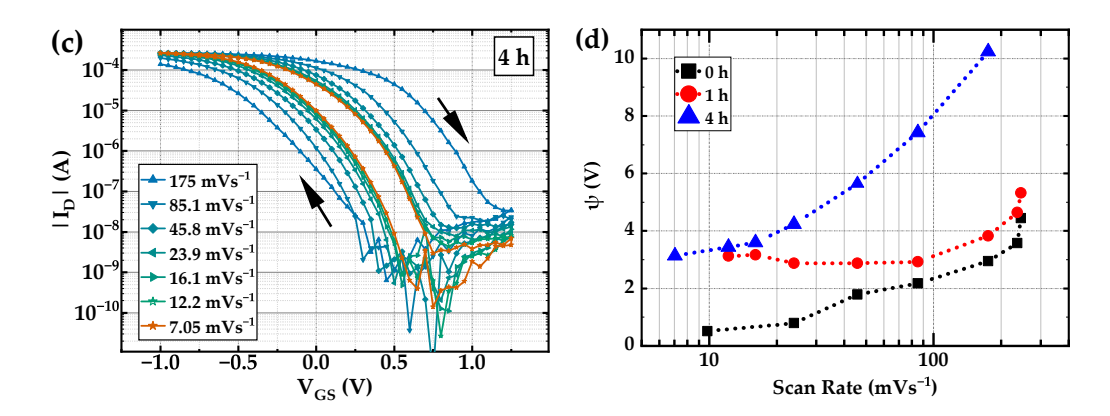


Figure 3. (a–c) Scan rate-dependent transfer curve measurements for OECTs where the PEDOT:Tos film is annealed for 0, 1, and 4h, respectively. (d) Hysteresis strength  $\psi$  plotted against the scan rates. The kinetic hysteresis strengths (at higher scan rates) increase with increasing annealing time. Non-kinetic hysteresis appears fastest in the 1 h-annealed film. Further, the 1 and 4 h-annealed devices show similar non-kinetic hysteresis ( $\psi \approx 3 \, \text{V}$ ), whereas the non-annealed device shows rather small non-kinetic hysteresis ( $\psi = 0.51 \, \text{V}$ ). Here, W, L, g = 150  $\mu$ m, 150  $\mu$ m, 50  $\mu$ m; V<sub>D</sub> = -0.2 V; the film thicknesses for 0, 1, 4h annealing are 103, 119, 141 nm, respectively.

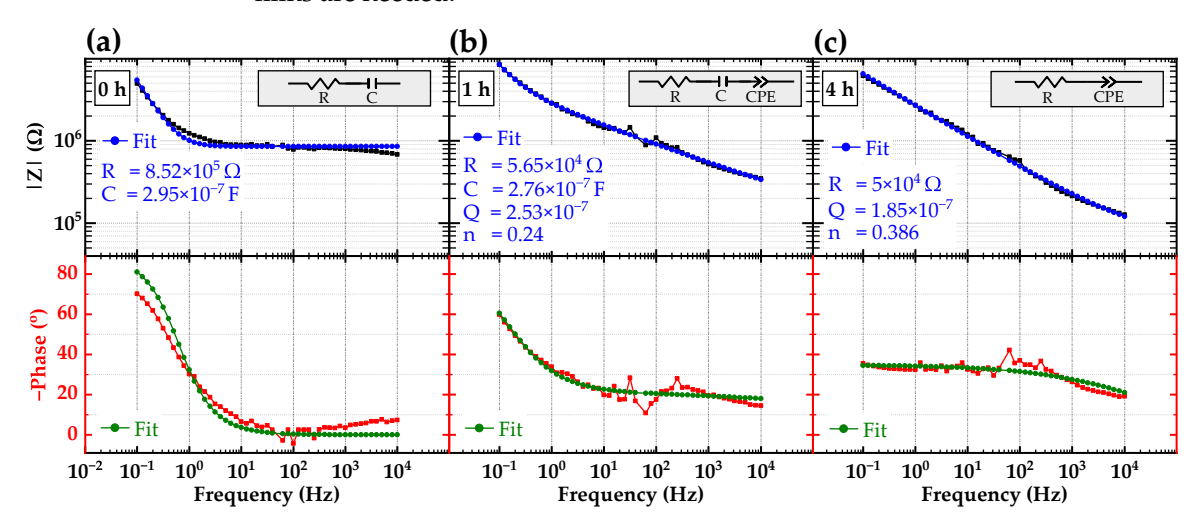
We performed impedance spectroscopy to gain more insight into the two regimes of hysteresis. Typically, the ionic circuit of an OECT is represented by a series circuit of a resistor and capacitors. The resistor accounts for the electrolyte resistance, while the capacitors represent the gate electrolyte and channel electrolyte interfaces. The capacitance of the gate is usually significantly larger and, hence, negligible in the series connection. One can also include a resistor parallel to the capacitor to include Faradaic processes. The ideal capacitor is a simplification, and usually, more complex models need to be used to describe all possible processes (e.g., accounting for different types of ions, their velocity distribution [4], and the non-uniformity of the electrode materials). Furthermore, the description of the electrode by means of a resistor is a simplification, as diffusion in an electrolyte is in general described by a Warburg element (behaving like a resistor at very low frequency and absorbing boundaries [26]).

Figure 4 depicts the impedances (source and drain at the same potential and impedance measured to the gate) of all the annealed devices, with the fitting circuit contained as inlets. For non-annealed devices (0 h), the impedance of the channel is mainly described by a pure resistor representing a Faradaic electrode with a capacitive contribution at only a very low frequency (presumably originating from the Warburg element describing the ion migration in the electrolyte). Therefore, it will mostly show kinetic hysteresis (the higher the sweep rate, the stronger the hysteresis is), which is in line with our observations. Moreover, the contribution of the capacitance to the impedance was small, and hence, the kinetic hysteresis was predicted to be the smallest for the non-annealed devices.

If the devices were annealed (1,4h), the impedance response transformed into the response of a constant phase element (CPE). For the 1 h-annealed device, an additional capacitor was required with the CPE to capture the response. The C and CPE in series imply that only the electrostatic process is there at the beginning. Thus, the electronic–ionic coupling would happen via the same states, but, e.g., the energies of these states change upon annealing, making a Faradaic process possible. With increasing annealing time, the slope in the Bode plot increased, meaning that the electrode was becoming more capacitive (hence, the kinetic hysteresis of the 4h device will be the strongest). However, the change from a Faradaic to non-Faradaic response explains the different strength of the kinetic hysteresis at high scan rates; still, it does not explain the origin of the non-kinetic hysteresis at low scan rates. The pronounced non-kinetic hysteresis ( $\psi \approx 3 \, \text{V}$ ) only occurred in the device with a capacitive character, while the non-annealed device was primarily resistive and only showed very low non-kinetic hysteresis ( $\psi = 0.51 \, \text{V}$ ), the origin of which still

Appl. Sci. **2023**, 13, 5754 7 of 11

remains elusive. The CPE in the impedance spectra tells us that the annealed PEDOT:Tos devices possessed a distribution of states at the interface between the electrolyte and the OMIEC, which is possibly connected to the appearance of the non-kinetic hysteresis. This transition in the impedance response of the PEDOT:Tos film is connected to the annealing-induced polymerization. We speculated that this polymerization process might trigger a demixing of the two components (PEDOT and Tos), similar to PEDOT:PSS [27], where, e.g., PSS-rich domains might act as deep trap states (as described by the CPE). However, to analyze this in more detail, further studies on the micro- and nano-scale formation of such films are needed.



**Figure 4.** Impedance measurements of OECTs employing PEDOT:Tos films annealed for 0,1,4 h. The corresponding fitting circuits and parameters are given as insets. The non-annealed device shows mostly a Faradaic response, which changes to non-Faradaic responses after annealing. The phase also indicates that the capacitances rapidly increase upon annealing. Here, W, L,  $g = 150 \,\mu\text{m}$ ,  $150 \,\mu\text{m}$ ,  $50 \,\mu\text{m}$ ; the thicknesses are 103, 119, 141 nm for thermal annealing of 0, 1, 4 h, respectively (a–c). The measurements were taken in potentiostatic mode with the source and drain shorted, with an RMS amplitude of 10 mV and without any DC offset. The instabilities around the  $50 \, \text{Hz}$  range probably originate due to the non-standard cables connecting the measurement setup inside the glovebox to the standard Autolab cables situated outside the glovebox.

#### 4. Summary

In this work, we demonstrated a fully photopatternable PEDOT:Tos OECT showing excellent bias stress stability, and we adopted a scan-rate-dependent measurement scheme to illustrate the kinetic and non-kinetic hysteresis. A strong enhancement of both could be revealed by thermal annealing, and we utilized impedance analysis to explain the changes in the two hysteresis regimes upon annealing. PEDOT:Tos was presumably well-mixed for non-annealed samples (all states were equivalent and had no dopant-rich or -poor domains), showing Faradaic behavior. Annealing fostered further polymerization of PEDOT, which might cause the demixing of PEDOT and Tos [23], showing a non-Faradaic behavior. Similar to PEDOT:PSS, ions might become trapped (represented by a CPE), causing an increased capacitance [27].

This work illustrated that PEDOT:Tos films employing solid electrolytes could be viable for applications where reliable long operation cycles are desired. A  $V_{GS}$  scan-rate-dependent measurement scheme captured the effects of the changing material properties on the device performances. This work further illustrated a simple process modification in thermal annealing to achieve varying hysteresis levels without changing the starting material, suitable for neuromorphic applications utilizing hysteresis [13,14]. While this work clearly distinguished between the non-kinetic and kinetic regimes of hysteresis, the true origin of the non-kinetic hysteresis remains open for investigation. In particular, further studies on micro- and nano-scale changes in PEDOT:Tos films upon annealing will

Appl. Sci. 2023, 13, 5754 8 of 11

provide valuable insights. If deep defects indeed cause the observed changes in hysteresis, annealing could pave the way to quantify and assess the effect of defect states on the OECTs' properties.

**Author Contributions:** R.S.: conceptualization, methodology, investigation, formal analysis, data curation, visualization, writing—original draft preparation. L.M.B.: methodology, formal analysis, software, writing—review and editing, supervision. A.W.: formal analysis, writing—review and editing, supervision. H.K.: project administration, resources, writing—review and editing, supervision. K.L.: validation, writing—review and editing, supervision. All authors have read and agreed to the published version of the manuscript.

**Funding:** Lukas M. Bongartz and Hans Kleemann are grateful for funding from the German Research Foundation (DFG) under the grant KL 2961/5-1. The authors also thank the Bundesministerium für Bildung und Forschung (BMBF) for funding from the project BAYOEN (01IS21089) and EC/SAB for funding in the ESF-Project "Re-Learning" (Funding No. 100382146).

Institutional Review Board Statement: Not applicable.

**Informed Consent Statement:** Not applicable.

Data Availability Statement: All data related to this article are available upon request.

**Conflicts of Interest:** The authors declare no conflict of interest.

## Appendix A.

Appendix A.1. Effect of Post-Polymerization Annealing on PEDOT:Tos Films

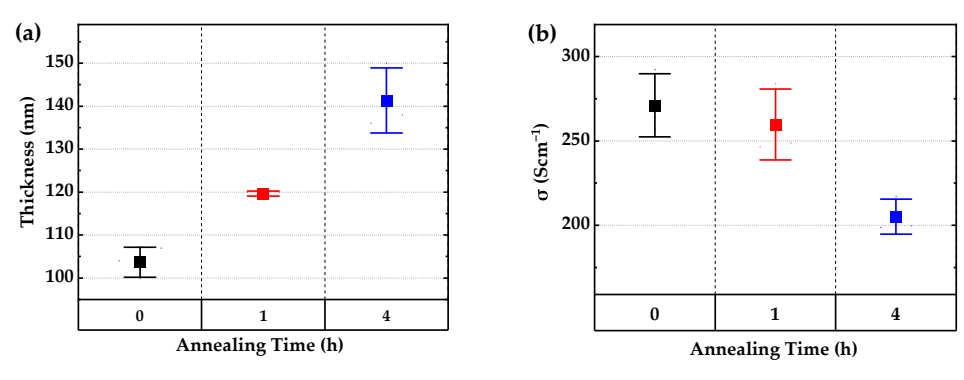


**Figure A1.** Effect of thermal annealing on the (a) thickness and (b) conductivity of PEDOT:Tos films. The bars represent standard deviations from the mean values. The adopted annealing temperature is 70 °C These results are in line with previous experiments [23].

Appendix A.2. Figure of Merits of the Fabricated Devices

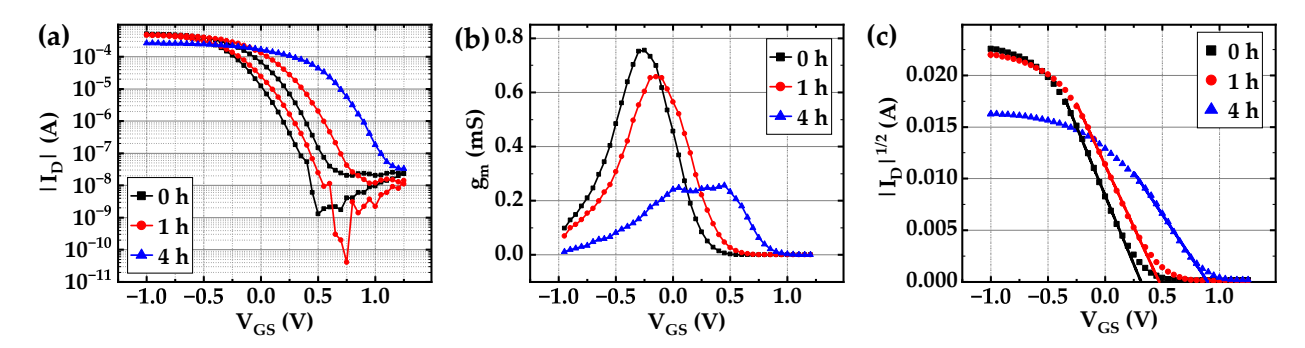


**Figure A2.** (a) Transfer curves, (b) peak transconductances (ON to OFF sweep), and (c) extracted threshold voltages (ON to OFF sweep) for OECTs annealed for 0, 1, 4 h. The annealing temperature is at 70 °C. Here, W, L,  $g = 150 \,\mu m$ ,  $150 \,\mu m$ ,  $50 \,\mu m$ ;  $V_{DS} = -0.2 \,V$ ; the thicknesses are 103, 119, 141 nm for thermal annealing of 0, 1, 4 h, respectively. The comparison is for a scan rate of  $\approx 175 \,\mathrm{mV \, s^{-1}}$ .

Appl. Sci. 2023, 13, 5754 9 of 11

## Appendix A.3. Hysteresis Windows

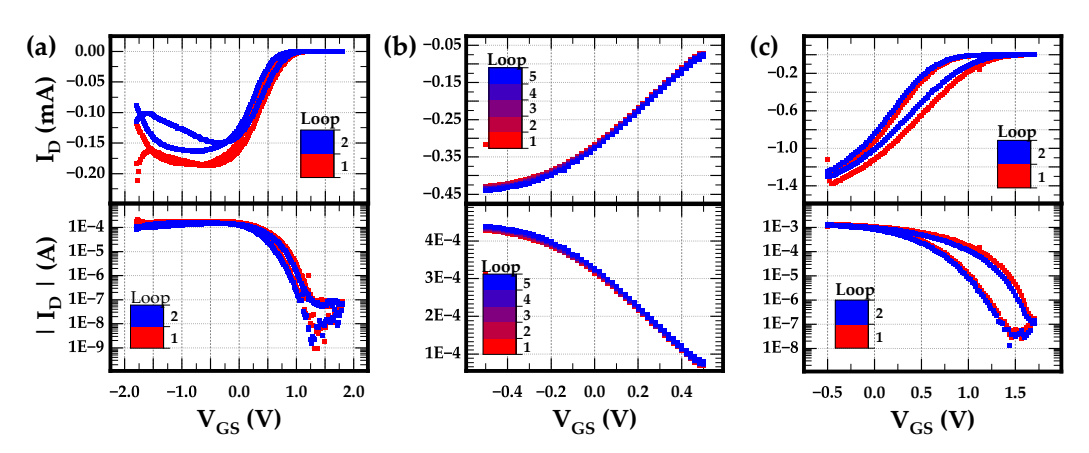


**Figure A3.** Changes of hysteresis for different  $V_{GS}$  scan windows: (a) the scan window is too high, causing device degradation; (b) the scan window is too small to observe any hysteresis; (c) the scan window captures the complete switching ON or OFF of the device, and the hysteresis strength does not increase for a further increase of the  $V_{GS}$  window [19].

## Appendix A.4. Current Stress

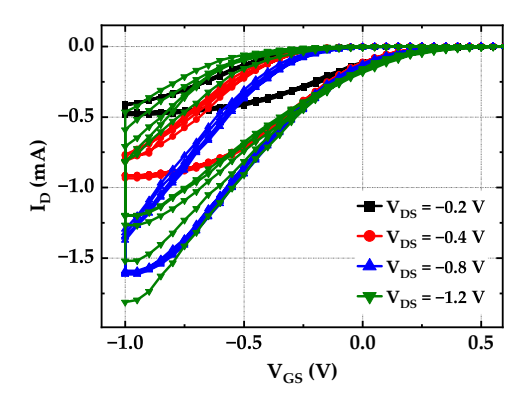


**Figure A4.** Current stress in OECTs, with no current stress visible at  $V_{DS} = -0.2$  V. Here, W, L, g, d = 150  $\mu$ m, 150  $\mu$ m, 50  $\mu$ m, and 103 nm. The annealing time is 0 h; the scan speed is  $\approx$ 245 mV s<sup>-1</sup>.

# Appendix A.5. Device Stability during Measurements

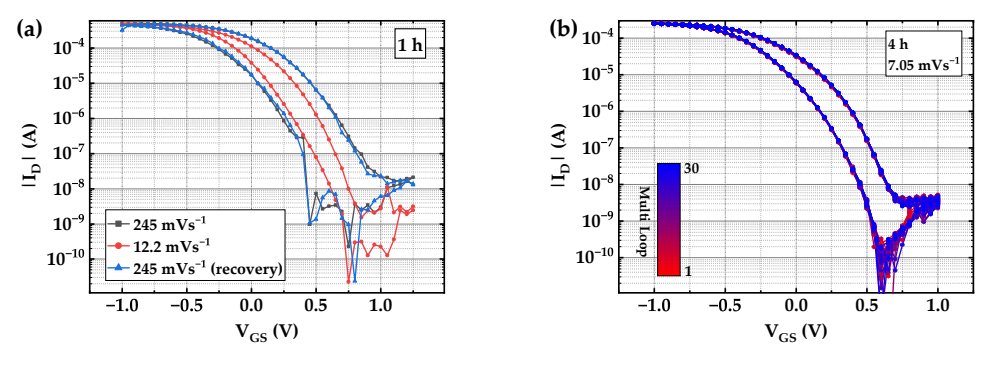


Figure A5. (a) Initial and final measurements for scan-rate-dependent measurement scheme for 1h annealed device. A recovery measurement depicts that the device can switch between different regimes of hysteresis when the bias stress is avoided by providing pauses. (b) A thirty-loop saturating hysteresis measurement for the 4h-thermally annealed film showing impressive consistency. The measurement duration is  $\approx$ 7 h, with no visible bias stress as the scan speed for such a measurement is significantly slower. Here, the devices have dimensions of W, L, g = 150  $\mu$ m, 150  $\mu$ m, 50  $\mu$ m;  $V_D = -0.2 \, V$ . The thicknesses are 119, 141 nm for thermal annealing of 1,4 h, respectively.

Appl. Sci. 2023, 13, 5754 10 of 11

#### References

1. Rivnay, J.; Leleux, P.; Ferro, M.; Sessolo, M.; Williamson, A.; Koutsouras, D.A.; Khodagholy, D.; Ramuz, M.; Strakosas, X.; Owens, R.M.; et al. High-performance transistors for bioelectronics through tuning of channel thickness. *Sci. Adv.* 2015, 1, e1400251. [CrossRef] [PubMed]

- 2. Jo, Y.J.; Kim, H.; Ok, J.; Shin, Y.J.; Shin, J.H.; Kim, T.H.; Jung, Y.; Kim, T.i. Biocompatible and biodegradable organic transistors using a solid-state electrolyte incorporated with choline-based ionic liquid and polysaccharide. *Adv. Funct. Mater.* **2020**, 30, 1909707. [CrossRef]
- 3. Strakosas, X.; Bongo, M.; Owens, R.M. The organic electrochemical transistor for biological applications. *J. Appl. Polym. Sci.* **2015**, 132, 41735. [CrossRef]
- 4. Tseng, H.; Cucchi, M.; Weissbach, A.; Leo, K.; Kleemann, H. Membrane-Free, Selective Ion Sensing by Combining Organic Electrochemical Transistors and Impedance Analysis of Ionic Diffusion. *ACS Appl. Electron. Mater.* **2021**, *3*, 3898–3903. [CrossRef]
- 5. Van De Burgt, Y.; Lubberman, E.; Fuller, E.J.; Keene, S.T.; Faria, G.C.; Agarwal, S.; Marinella, M.J.; Alec Talin, A.; Salleo, A. A non-volatile organic electrochemical device as a low-voltage artificial synapse for neuromorphic computing. *Nat. Mater.* **2017**, 16, 414–418. [CrossRef] [PubMed]
- Gerasimov, J.Y.; Gabrielsson, R.; Forchheimer, R.; Stavrinidou, E.; Simon, D.T.; Berggren, M.; Fabiano, S. An evolvable organic electrochemical transistor for neuromorphic applications. Adv. Sci. 2019, 6, 1801339. [CrossRef]
- 7. Cucchi, M.; Gruener, C.; Petrauskas, L.; Steiner, P.; Tseng, H.; Fischer, A.; Penkovsky, B.; Matthus, C.; Birkholz, P.; Kleemann, H.; et al. Reservoir computing with biocompatible organic electrochemical networks for brain-inspired biosignal classification. *Sci. Adv.* 2021, 7, eabh0693. [CrossRef]
- 8. Petrauskas, L.; Cucchi, M.; Grüner, C.; Ellinger, F.; Leo, K.; Matthus, C.; Kleemann, H. Nonlinear Behavior of Dendritic Polymer Networks for Reservoir Computing. *Adv. Electron. Mater.* **2022**, *8*, 2100330. [CrossRef]
- 9. Paulsen, B.D.; Tybrandt, K.; Stavrinidou, E.; Rivnay, J. Organic mixed ionic–electronic conductors. *Nat. Mater.* **2020**, *19*, 13–26. [CrossRef]
- Friedlein, J.T.; McLeod, R.R.; Rivnay, J. Device physics of organic electrochemical transistors. Org. Electron. 2018, 63, 398–414.
  [CrossRef]
- 11. Khodagholy, D.; Rivnay, J.; Sessolo, M.; Gurfinkel, M.; Leleux, P.; Jimison, L.H.; Stavrinidou, E.; Herve, T.; Sanaur, S.; Owens, R.M.; et al. High transconductance organic electrochemical transistors. *Nat. Commun.* **2013**, *4*, 2133. [CrossRef] [PubMed]
- 12. Zeglio, E.; Inganäs, O. Active materials for organic electrochemical transistors. *Adv. Mater.* **2018**, *30*, 1800941. [CrossRef] [PubMed]
- 13. Winther-Jensen, B.; Kolodziejczyk, B.; Winther-Jensen, O. New one-pot poly (3, 4-ethylenedioxythiophene): Poly (tetrahydrofuran) memory material for facile fabrication of memory organic electrochemical transistors. *APL Mater.* **2015**, *3*, 014903. [CrossRef]
- 14. Ji, X.; Paulsen, B.D.; Chik, G.K.; Wu, R.; Yin, Y.; Chan, P.K.; Rivnay, J. Mimicking associative learning using an ion-trapping non-volatile synaptic organic electrochemical transistor. *Nat. Commun.* **2021**, *12*, 2480. [CrossRef]
- 15. Brooke, R.; Cottis, P.; Talemi, P.; Fabretto, M.; Murphy, P.; Evans, D. Recent advances in the synthesis of conducting polymers from the vapour phase. *Prog. Mater. Sci.* **2017**, *86*, 127–146. [CrossRef]
- 16. Khodagholy, D.; Curto, V.F.; Fraser, K.J.; Gurfinkel, M.; Byrne, R.; Diamond, D.; Malliaras, G.G.; Benito-Lopez, F.; Owens, R.M. Organic electrochemical transistor incorporating an ionogel as a solid state electrolyte for lactate sensing. *J. Mater. Chem.* **2012**, 22, 4440–4443. [CrossRef]
- Andersson Ersman, P.; Lassnig, R.; Strandberg, J.; Tu, D.; Keshmiri, V.; Forchheimer, R.; Fabiano, S.; Gustafsson, G.; Berggren, M. All-printed large-scale integrated circuits based on organic electrochemical transistors. *Nat. Commun.* 2019, 10, 5053. [CrossRef]
- 18. Zabihipour, M.; Lassnig, R.; Strandberg, J.; Berggren, M.; Fabiano, S.; Engquist, I.; Andersson Ersman, P. High yield manufacturing of fully screen-printed organic electrochemical transistors. *npj Flex. Electron.* **2020**, *4*, 15. [CrossRef]
- 19. Weissbach, A.; Bongartz, L.M.; Cucchi, M.; Tseng, H.; Leo, K.; Kleemann, H. Photopatternable solid electrolyte for integrable organic electrochemical transistors: Operation and hysteresis. *J. Mater. Chem. C* **2022**, *10*, 2656–2662. [CrossRef]
- 20. Kaphle, V.; Liu, S.; Keum, C.M.; Lüssem, B. Organic electrochemical transistors based on room temperature ionic liquids: Performance and stability. *Phys. Status Solidi (a)* **2018**, 215, 1800631. [CrossRef]
- 21. Höppner, M.; Kneppe, D.; Kleemann, H.; Leo, K. Precise patterning of organic semiconductors by reactive ion etching. *Org. Electron.* **2020**, *76*, 105357. [CrossRef]
- 22. Winther-Jensen, B.; West, K. Vapor-phase polymerization of 3, 4-ethylenedioxythiophene: A route to highly conducting polymer surface layers. *Macromolecules* **2004**, *37*, 4538–4543. [CrossRef]
- 23. Zuber, K.; Shere, H.; Rehmen, J.; Wheaton, V.; Fabretto, M.; Murphy, P.J.; Evans, D.R. Influence of postsynthesis heat treatment on vapor-phase-polymerized conductive polymers. *ACS Omega* **2018**, *3*, 12679–12687. [CrossRef] [PubMed]
- 24. Cucchi, M.; Weissbach, A.; Bongartz, L.M.; Kantelberg, R.; Tseng, H.; Kleemann, H.; Leo, K. Thermodynamics of organic electrochemical transistors. *Nat. Commun.* **2022**, *13*, 4514. [CrossRef] [PubMed]
- 25. Bongartz, L.M.; Weissbach, A.; Cucchi, M.; Leo, K.; Kleemann, H. Temperature-Dependence of All-Solid-State Organic Electrochemical Transistors. In Proceedings of the 2022 IEEE International Conference on Flexible and Printable Sensors and Systems (FLEPS), Vienna, Austria, 10–13 July 2022; pp. 1–4. [CrossRef]

Appl. Sci. 2023, 13, 5754

26. Bisquert, J. Theory of the Impedance of Electron Diffusion and Recombination in a Thin Layer. *J. Phys. Chem. B* **2002**, *106*, 325–333. [CrossRef]

27. Volkov, A.V.; Wijeratne, K.; Mitraka, E.; Ail, U.; Zhao, D.; Tybrandt, K.; Andreasen, J.W.; Berggren, M.; Crispin, X.; Zozoulenko, I.V. Understanding the capacitance of PEDOT: PSS. *Adv. Funct. Mater.* **2017**, 27, 1700329. [CrossRef]

**Disclaimer/Publisher's Note:** The statements, opinions and data contained in all publications are solely those of the individual author(s) and contributor(s) and not of MDPI and/or the editor(s). MDPI and/or the editor(s) disclaim responsibility for any injury to people or property resulting from any ideas, methods, instructions or products referred to in the content.